2023

Co–MoCx supported on N-doped CNTs for efficient hydrogen evolution reaction under alkaline medium conditions†

Chi Wing, Alex Tsang

Dawson Wai Shun Suen

NJC

ROYAL SOCIETY OF CHEMISTRY

PAPER

View Article Online
View Journal

Cite this: DOI: 10.1039/d3nj03937d

Co–MoC_x supported on N-doped CNTs for efficient hydrogen evolution reaction under alkaline medium conditions†

Weilin Shen,‡[a] Dawson Wai-Shun Suen,‡[b] Eric Tung-Po Sze,[c] Xiao Chen, *[a] Changhai Liang [a] and Chi-Wing Tsang *[b]

Received 22nd August 2023,
Accepted 17th October 2023

DOI: 10.1039/d3nj03937d

rsc.li/njc

The water splitting reaction has the potential to be a sustainable and environmentally friendly way of producing hydrogen as a fuel source, which is an important step in reducing our reliance on fossil fuels and mitigating climate change. Currently, most commonly used catalysts for water splitting are based on precious metals such as platinum and iridium, which are expensive and scarce. Therefore, finding new catalysts that are low-cost, abundant and efficient is of great importance for making water splitting economically viable on a large scale. It was found that pairing up Co nanoparticles (NPs) with MoC_x boosted the hydrogen evolution reaction (HER) activity by more than 2-fold (η_{10} = 130 mV, Tafel slope = 156.08 mV dec^{-1}), compared with the pure Co NPs supported on N-doped carbon (η_{10} = 337 mV) under alkaline medium conditions. Its activity is comparable to those of Pt single-atom catalysts (SACs) supported on a mesoporous carbon matrix. The good activity may be due to the modification of the D-band of Co by Mo doping and the relatively high electrochemically active surface area (ECSA) of 477.25 cm^2, which is comparable to those of Ru SAC materials.

Introduction

Excessive emissions of carbon dioxide have a significant negative impact on the environment, such as global warming.[1] Anthropogenic carbon emissions have led to a 1.1 °C increase in global temperature with reference to the pre-industrial level, which is mainly due to the combustion of fossil fuels. Hydrogen is a clean energy carrier,[2] which could be a solution to this problem since it produces zero carbon emissions and electricity, water and heat are its only products when it is used in fuel cells. To meet the era of the hydrogen economy, society needs to solve several technical challenges urgently, *i.e.*, production, transportation and storage of hydrogen. Hydrogen production remains the biggest hurdle in sustainably closing the hydrogen cycle. As of 2021, the world's hydrogen production is mainly carried out by thermochemical methods. To eliminate the depletion of fossil fuel resources, using water resources could be the key to limiting the global temperature increase to within 1.5 °C. However, water electrolysis processes have long been criticized because of their general sluggish rates, high electricity consumption and the use of expensive platinum (Pt) electrodes, which made them not practical for commercial use.[2] Therefore, reducing overpotentials and replacing Pt with other more economically viable metals have become effective strategies for driving the green hydrogen energy transition.

To date, the best record to use a non-Pt-based electrode in the hydrogen evolution reaction (HER) through water electrolysis is held by Ru nanoparticles (NPs) supported on a 2D N-doped carbon structure, with an overpotential of 17 mV at 10 mA cm^{-2}.[3] However, due to technical bottlenecks such as high cost, scarcity and limited stability, there is still a long way to go towards its commercialization. Base metal catalysts such as Cu, Co, Mo, Fe and Ni are more economically viable but they generally exhibit a much lower stability and sluggish reaction rate. In recent years, Yan and Luo *et al.* have synthesized a number of non-precious metal catalysts, such as Ni-BTC,[4] MSi[5] and topological 1T′-$MoTe_2$,[6] all of which have good stability. Recent strategies to increase the intrinsic activity of active sites include (1) downsizing the NPs to increase the surface area and the amount of active sites,[7] as in single-atom catalysts (SACs),

[a] State Key Laboratory of Fine Chemicals, Laboratory of Advanced Materials and Catalytic Engineering, School of Chemical Engineering, Dalian University of Technology, Dalian 116012, China. E-mail: xiaochen@dlut.edu.cn
[b] Faculty of Science and Technology, Technological and Higher Education Institute of Hong Kong (THEi), Hong Kong 999077, China. E-mail: ctsang@thei.edu.hk; Web: https://www.thei.edu.hk/staff/details/chi-wing-alex-tsang; Fax: +852-2176-1554
[c] School of Science and Technology, Hong Kong Metropolitan University, Hong Kong Special Administrative Region, Hong Kong, China

† Electronic supplementary information (ESI) available. See DOI: https://doi.org/10.1039/d3nj03937d

‡ Equal contributions.

or atomically dispersed sites on carbon supports and (2) creating dual-active sites for water dissociation and surfaces for H_{ads} adsorption, respectively. However, so far, no clear correlation between size and reactivity for NPs has been found. For example, in acidic media, while Pt_{nano} with a size of 230 nm showed excellent HER activity, Pt_{10} monodisperse nano-clusters showed only a much reduced catalytic activity.[8] Clearly, the HER performance cannot be boosted by just the size factor but may require multiple strategies.

Specifically, SACs refer to the catalysts with NPs that are downsized to the atomic level, where the atoms are usually stabilized by neighboring surface atoms (*e.g.* N, O and P) *via* covalent or ionic interactions. Since the discovery of the first SACs (Pt_1/FeO_x),[9] various SACs exhibiting superior activities in many catalytic conversions, such as hydrogenation, reduction, oxidation, hydroformylation, electrocatalysis, *etc.*, have been discovered. In the HER, for example, Pt SACs prepared by atomic layer deposition supported on nitrogen-doped graphene nanosheets showed an η_{10} of 50 mV and a mass activity of 10.1 A mg_{metal}^{-1}, which is 37.4 times greater than the mass activity of the commercial Pt/C catalyst (mass activity = 0.27 A mg_{metal}^{-1}).[10] One example of using Pt-based catalysts for the HER performed under alkaline conditions was reported by Lou *et al.*, in an attempt to modulate and stabilize the isolated Pt atoms within the mesoporous carbon matrix.[11] However, a much higher η_{10} of 139 mV and a Tafel slope of 73.6 mV dec^{-1} were reported. Nowadays, the reported efficient SACs as HER catalysts using are mostly comprised of precious metals and related derivatives, where most of them were studied under acidic conditions. It is thus highly desirable to investigate HER catalysts under alkaline conditions using non-precious metals.

In search of a suitable catalyst for the water cleavage reaction during the ammonia borane hydrolysis reaction under alkaline conditions, we have previously synthesized a type of Co NPs/Co SAC catalyst with metal loading (25 wt%) by a facile one-pot pyrolysis method. The Co ions were pre-mixed with graphene-like C_3N_4 (g-C_3N_4) *via* N coordination followed by a series of pyrolysis steps to reach 800 °C. These Co NPs supported on carbon nanotubes (CNTs) doped with the atomically dispersed CoN_4 moiety demonstrated an η_{10} of 143 mV with a Tafel slope of 66.82 mV dec^{-1} in the alkaline HER reaction, which showed a great improvement compared to regular Co NPs supported on N-doped carbon (η_{10} = 337 mV) under alkaline medium conditions.[12] To further increase the HER reactivity of Co-based catalysts, we propose to investigate the D-band model in a dual-atom system. Molybdenum derived and related catalysts such as CoMoP@C,[13] CoMo bimetallic carbide,[14] CoMo bimetallic nitride[15,16] and CoMo bimetallic sulphide[17] are effective towards the HER and some of them are even comparable to commercial Pt/C catalysts. Furthermore, it was known that Mo-doping to single atom Co_4N nanosheets can further fine-tune the ΔG_{H^*} to be much closer to the thermoneutral level in the Volmer step during the acidic HER.[18] Therefore, we have further modified Co NPs with Mo doping to obtain Co–MoC_x NPs and it was found that the η_{10} was found to be 130 mV with a Tafel slope of 156.08 mV dec^{-1}, which is comparable to Pt SACs supported on a mesoporous carbon matrix.[11] The good activity may be due to the modification of the D-band of Co by Mo doping and the relatively high electrochemically active surface area (ECSA) of 477.25 cm^2 (which is comparable to those of Ru SAC materials).[19]

Experimental

Materials

Bis(acetylacetonato)dioxomolybdenum(VI) ($MoO_2(acac)_2$, Sigma-Aldrich), dicyandiamide ($C_2H_4N_4$, DCD, Sigma-Aldrich), cobalt(II) acetylacetonate ($Co(acac)_2$, Sigma-Aldrich), cupric(II) acetylacetonate ($Cu(acac)_2$, Sigma-Aldrich), manganese(III) acetylacetonate ($Mn(acac)_3$, Sigma-Aldrich), and polytetrafluoroethylene preparation ((PTFE), Aladdin) were purchased and used without further treatment.

Preparation of catalysts

Preparation of *melem*-C_3N_4 (DCD-350): dicyandiamide (80 g, 0.95 mol) was equally distributed in four porcelain crucibles and heated to 350 °C in a muffle furnace (Model: MTI OTF-1200X) for 2 h, where around 50 g of materials were obtained in each batch.

Preparation of citric acid solution (10 g L^{-1}): citric acid (10 g) was dissolved in 0.5 L of deionized water and diluted to 1 L using ethanol (95%). This citric acid will assist in the dispersion of the metals (Co and Mo) in *melem*-C_3N_4 as well as increase the specific surface areas of the carbonized catalysts.

Preparation of Co–MoC_x/N-doped carbon nanotubes (Co–MoC_x/N-CNTs): DCD-350 (10 g), $Co(acac)_2$ (0.1488 g, 0.5787 mmol) and $MoO_2(acac)_2$ (0.1019 g, 0.2893 mmol) were mixed and ground using a ball miller in a 1.5 h alternating motion cycle (*i.e.* changing the rotation direction every 5 min). The citric acid solution (6 mL) was subsequently added to the mixture and dried in an oven at 90 °C for 2–4 h until a constant mass was achieved. The resulting dried mixture was then placed in the ball miller for another 1.5 h alternating motion cycle before being transferred into a ceramic crucible and heated to 800 °C for 2 h at a heating rate of 2.6 °C min^{-1} under a steady stream of Ar (150 mL min^{-1}) to create an Ar atmosphere in a tube furnace and subsequently cooled down to room temperature by natural cooling. The overall yield of the catalyst was around 1 g, which was around 10% based on starting DCD-350. Co–Cu/N-CNTs and Co–Mn_xN_y/N-CNTs were also prepared by the same method using the corresponding metal salts, respectively.

Materials characterization of catalysts

X-Ray powder diffraction (XRD) was used for the phase identification of the crystalline carbonized material Co–MoC_x/N-CNTs. The defect types and quantities of the catalytic materials were determined by Raman spectroscopy. X-Ray photoelectron spectroscopy (XPS) was used to measure the valence-state of the elements of the catalytic materials. Scanning electron microscopy (SEM) was used to analyze the structural

morphology at the micro-scale, while high resolution transmission electron microscopy (TEM) was used to analyze the microstructure at the nano-scale. Brunauer–Emmett–Teller (BET) and Barrett–Joyner–Halenda (BJH) methods were used to determine the specific surface area and the pore size distribution of the catalytic materials, respectively. The details and models of the instrument were described in Section S1 in the ESI.†

The metal contents by mass of the as-synthesized catalysts were determined utilizing inductively coupled plasma optical emission spectroscopy (ICP-OES) on an Agilent 5110 ICP-OES device, where an Ar plasma source was used to excite atoms and/or ions. In a typical ICP-OES analysis, a 20 mg sample was dissolved in 50 mL of a 2 M HCl/HNO_3 mixture (with a mole ratio of HCl to HNO_3 as 3 : 1) under hydrothermal conditions (180 °C).[20] Elemental concentrations for Co and Mo were determined by measuring the Co emission line at 238.9 and 228.6 nm as well as the Mo emission line at 202 and 204.6 nm and taking the average intensity between the two wavelengths of each metal, respectively. The samples were diluted to the range of 2 to 40 ppm by diluting the supernatant five times (diluting to 250 mL with deionized water) upon filtration. The calibration curves of Co and Mo from 0 to 40 ppm were prepared for quantification. Multi-point calibration curves were constructed from certified standards (TraceCERT® from Sigma Aldrich). The sample transport system utilized a cyclonic spray chamber equipped with a Meinhard nebulizer, with instrument parameters set as follows: plasma flow rate, 12.0 L Ar (g) min^{-1}; auxiliary flow rate, 1 L Ar (g) min^{-1}; nebulizer flow rate, 0.7 L Ar (g) min^{-1}; power, 1200 W; and pump speed 12 rates per minute.

Electrochemical measurements of materials

All electrochemical measurements were conducted at room temperature using a CS310H electrochemical workstation (Wuhan Corrtest Co., Ltd) equipped with a three-electrode system. The working electrode was prepared by loading catalyst ink onto a nickel foam (NF) with a size of 1 cm × 1 cm. All measurements are carried out at the same optimized metal loading weight of 2 mg cm^{-2}. The overpotential (η) was calculated using the equation: $\eta = E_{RHE} - 0$ V. The catalyst ink was prepared by dispersing 20 mg of catalyst in 2.0 mL of a solution containing 0.2 mL of isopropanol, 1.8 mL of H_2O and 44 mg of 5 wt% PTFE solution followed by ultrasonication for 40 min. An Hg/HgO electrode was used as the reference electrode and a carbon rod was used as the counter electrode. For convenience, all measured potentials in our work were calibrated to a reversible hydrogen electrode (RHE) according to $E_{RHE} = E_{Hg/HgO} + 0.059pH + E^0_{Hg/HgO}$ (where E_{RHE} is the converted potential *vs.* RHE, $E_{Hg/HgO}$ is the experimental potential measured against a Hg/HgO reference electrode and $E^0_{Hg/HgO}$ = 0.098 V at ambient temperature) unless it was represented individually. Then, all of the potentials reported in our work were corrected with IR compensation (where R is the series resistance arising from catalysts, electrolyte and contact resistance of the setup, measured by electrochemical impedance spectroscopy (EIS)). The electrocatalytic HER performances of all synthesized electrocatalysts were studied in an alkaline medium (1.0 M KOH, pH = 14), therefore, $E_{RHE} = E_{Hg/HgO} + 0.924$. Before conducting any electrochemical tests, all catalysts were pretreated by cycling 30 times through the potential window of −1.124–−0.924 V *vs.* Hg/HgO at a scan rate of 50 mV s^{-1} to reach a stable state. Linear sweep voltammetry (LSV) measurements were performed at a scan rate of 1 mV s^{-1}. EIS results were collected within the frequency range of 100 kHz–0.1 Hz at an overpotential of 200 mV. The ECSA of the catalyst is proportional to the double-layer capacitance (C_{dl}) of the catalyst.[21] The C_{dl} values of electrocatalysts were investigated using cyclic voltammetry (CV) measurements in a non-faradaic region (in this work, −0.824 to −0.724 V *vs.* Hg/HgO) at the various scan rates of 20, 40, 60, …, 200 mV s^{-1}. Faradaic efficiency (FE) was calculated by recording the reaction time and measuring the volume of gas generated by electrolyzing water, when a chrono potentiometry (CP) scan was performed at a constant current density of 25 mA cm^{-2}.

Results and discussion

Phase analysis of materials

Samples of freshly as-prepared catalysts were subjected to XRD to quantify the microcrystalline phase and crystallinity of the metal nanoparticles. The XRD pattern of Co–MoC_x/N-CNTs is shown in Fig. 1c, where intense and sharp diffraction peaks are indicative of well-defined crystalline structures. It is known that the main components of Co–MoC_x/N-CNTs are metallic Co and carbides of molybdenum, in which carbides of molybdenum belong to a hexagonal crystal system. Diffraction peaks corresponding to the Co (111), (200) and (220) planes (at 2θ values of 44.3, 51.6 and 75.9°, respectively) of the Co FCC phase were present and were consistent with the ICDD (the International Centre for Diffraction Data) power diffraction file (ICDD No. 15-0806). The broad and blunt peak at a 2θ value of 20° is generated by amorphous carbon diffraction, where the obvious broad peak at a 2θ value of 26° corresponds to the graphitized carbon and is also indexed well in the PDF card of ICDD No. 75-1621. When $MoO_2(acac)_2$ was replaced with $Cu(acac)_2$ or $Mn(acac)_2$, respectively, no pure corresponding carbides were

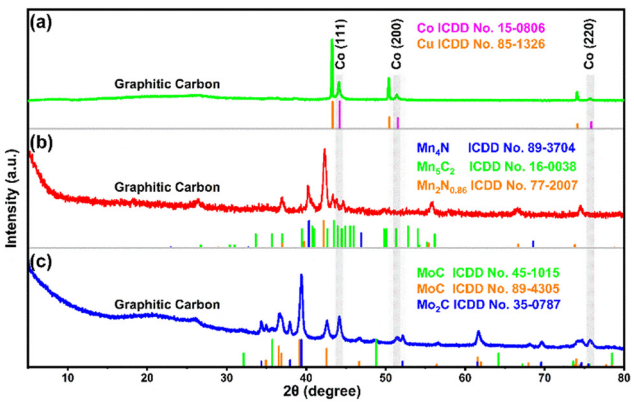

Fig. 1 X-ray diffraction patterns of (a) Co–Cu/N-CNT (b) Co–MnC_x-MnN_x/N-CNT and (c) Co–MoC_x/N-CNT samples.

obtained. The detailed phase analysis is shown in Fig. 1a and b. The diffraction peaks of metallic Co and the graphitized carbon can be observed as shown in Fig. 1a–c, indicating that Co is reduced, highlighting the presence of Co on N-CNTs.

Formation mechanism of the Co/N-CNT, Co–MoC_x/N-CNT, Co–Cu/N-CNT, and Co–Mn_xN_y/N-CNT

The formation mechanism of Co-catalyzed CNTs is likely to be different because of the typical growth of CNTs. During pyrolysis, Co single atoms (SAs) and NPs act as catalysts and the Co-g-C_3N_4 intermediate plays a key role in the formation of Co-N-CNTs. Although CNT formation with different transitional-metals under different conditions can be explained through different processes and mechanisms, due to their proximity on the periodic table, we believe that Co-CNTs share similar formation mechanisms with Ni-CNTs. Co SAs accelerate the formation of CNTs while stabilizing g-C_3N_4 and was therefore able to protect some of the g-C_3N_4 from decomposing. Essentially, at high temperatures of 700–900 °C, sheets of Co-g-C_3N_4 roll up due to the buildup of internal stress from the thermal movement of Co SA, thereby forming the bamboo-like structures.[22,23] This rolling up phenomenon will only occur when there exists a suitable concentration of Co SA within the g-C_3N_4 material, which was experimentally determined to be around 3%. We believe that the covalent bonding between Co atoms and g-C_3N_4 is weaker than the covalent bonding between Ni and g-C_3N_4. This is because unlike the case for Ni, where single atom aggregation was inhibited due to the strong covalent bonding between Ni and g-C_3N_4,[23] both Co SAs and NPs were detected in our catalyst. As determined by XANES analysis in our previous results, Co/N-CNTs could present certain amounts of Co-SAs on the CNT, together with the Co NPs.[24]

Under the same pyrolysis atmosphere, different metals with dicyandiamide may lead to different results. With 3% of metal salt (base on metal cations) added to DCD-350 (in excess), molybdenum carbides are preferentially formed, which is in accordance with the conditions reported for the ''urea glass'' technique.[25] On the other hand, manganese nitrides are exclusive species, with the formation of a small amount of manganese carbides. This mechanism is similar to the reported metal-urea complex decomposition,[26] where the metal-DCD salt first undergoes decomposition, followed by nitridation under the NH_3 atmosphere. For both Co and Cu, the NH_3 atmosphere is not concentrated enough to nitridify the metal species, thus pure Co^0 and Cu^0 were obtained for the Co/N-CNT and Co–Cu/N-CNT, in the form of small and homogeneously monodisperse NPs.

Electrochemical performance of materials

Over the past decade, numerous heterogeneous precious and non-precious metal NP catalysts such as Rh, Pt, Ir, Ru, Mo, Co, Fe, Ni and Cu have been explored to be active in the HER in alkaline electrolytes, where various strategies have been observed. These include the creation of ''dual-sites'' on the catalyst surface such as coupling Pt with an oxophilic metal for strong interaction with the OH_{ads} species. As a result, the Pt catalyst decorated with $Ni(OH)_2$ NPs increased the HER activity by 8 fold compared with Pt.[27] However, this method suffers from complicated synthetic steps and long-term stability due to the leakage and dissolution of $Ni(OH)_2$ NPs. Other strategies include the modification of the electronic structure of the metal NPs using the D-band theory. This involves the utilization of transition metal nitrides,[28] phosphides,[29] sulfides,[30] oxides[31] and carbides.[32] In these cases, improved HER performance compared to the pure metal NPs was observed. However, they exhibited sluggish H_2 production rate and lower cyclic stability. Thus, several technical challenges relating to activity and stability persist and consequently hamper the technological readiness of the HER, which include (i) how to increase the kinetics of the water-dissociation step by non-precious metals to be competitive with Pt-based catalysts' performance; (ii) how to design catalysts with optimal adsorption/desorption of adsorbed H species (H_{ads}); and (iii) how to increase the stability and efficiency of mass transport and electron transfer during electrolysis.

It was only until the recent emergence of SACs that the overpotential reached a very low value. However, the studies were mainly focused on Pt and Ru, while the development of non-precious metal SACs for the HER under alkaline conditions is still in its infancy.[33] For example, Pt SACs prepared by atomic layer deposition supported on nitrogen-doped graphene nanosheets showed an η_{10} of about 50 mV and a mass activity of 10.1 A mg_{metal}^{-1}, which is 37.4 times greater in activity than the commercial Pt/C catalyst (mass activity = 0.27 A mg_{metal}^{-1}).[10] Pt SACs supported on carbon nanospheres exhibited a small η_{10} of 38 mV with a small Tafel slope of 36 mV dec^{-1}, which is very similar to commercial Pt/C in terms of activity.[34] Nonetheless, the above successful HER examples mentioned above were performed in acidic media. One example of the HER performed under alkaline conditions was reported by Luo *et al.*, in an attempt to modulate and stabilize the isolated Pt atoms within the mesoporous carbon matrix.[11] However, a much higher η_{10} of 139 mV and a Tafel slope of 73.6 mV dec^{-1} were reported. In search of a suitable catalyst that could facilitate water dissociation for the hydrolysis of ammonia borane (AB), we found that non-precious metals such as Co NPs and Co SACs bifunctional catalysts (Co/CoN_x-CNT) can synergistically boost the rate by 2 fold, when compared with traditional metal NPs catalysts.[24] With the use of synchrotron radiation (SR) techniques, the existence of a single-atom active site was unequivocal and it was also postulated that HO*–(Co–N_4) was the active site for facile water adsorption and dissociation,[35] where the H_2O molecule has a larger adsorption energy on HO–Co_1–N_2 (0.94 eV) than on Pt(111) (0.46 eV) to form the H_2O–(HO–Co_1–N_2) intermediate. On the other hand, D-band center modulations have been known to effectively increase the HER rate. For example, the D-band of Co of Co_4N nanosheets can be tailored *via* transition metal doping, such as V and Mo doping. The Mo-doped Co_4N nanosheets displayed an overpotential of only 44 mV compared with 93 mV of Co_4N at 10 mA cm^{-2} in acidic media. The D-band was shifted more downward away from the Fermi level and the ΔG_{H^*} of Mo–Co_4N was calculated to be closer to the thermoneutral value (−0.21 eV) compared with −0.56 eV of

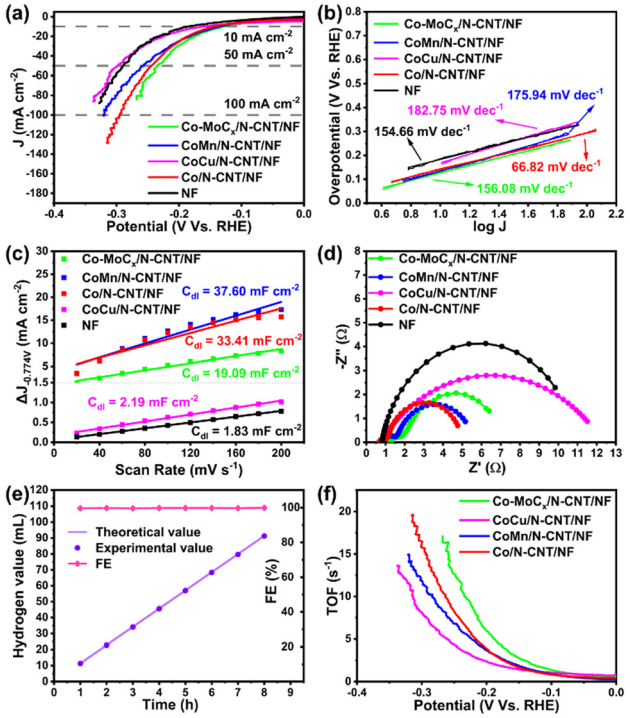

Fig. 2 (a) HER polarization curves of electrocatalysts, (b) the corresponding Tafel plots for different electrocatalysts, (c) the measured capacitive current density at −0.774 V *vs.* Hg/HgO as a function of the scan rate, used to indicate the electrochemically effective active surface area, (d) Nyquist plots of the different electrocatalysts at an overpotential of 200 mV. The fitted curves are presented by solid lines, (e) Faraday efficiency and experimental and theoretical amounts of H_2 catalyzed by Co–MoC_x/N-CNT/NF in 1.0 M KOH, respectively, at a fixed current density of 25 mA cm^{-2}, (f) TOF values as a function of the potential for electrocatalysts.

Co_4N nanosheets.[18] We therefore carried out the syntheses of a series of monometallic Co and bimetallic (Co–M, M = Mo, Cu, Mn) bifunctional catalysts and tested their HER reactivities. Fig. 2a shows the polarization curves of the catalyzed HER. The HER catalytic activity of these catalysts follows the sequence of Co–MoC_x/N-CNT/NF > Co/N-CNT/NF > Co–Mn_xN_y/N-CNT/NF > Co–Cu/N-CNT/NF ≈ NF. The Co/N-CNT/NF required an overpotential of 143 mV and 244 mV at 10 mA cm^{-2} and 50 mA cm^{-2}, respectively. The overpotential required for the bifunctional catalyst was slightly higher than that of the Co_1/CN catalyst[35] but was much lower than that of the regular Co NPs supported on N-doped carbon (η_{10} = 337 mV) under alkaline conditions.[12] In particular, Co–MoC_x/N-CNT/NF requires the lowest overpotentials of 130 mV and 234 mV to achieve the current densities of 10 mA cm^{-2} and 50 mA cm^{-2} respectively, while Co/N-CNT/NF, Co–Mn_xN_y/N-CNT/NF and Co–Cu/N-CNT/NF exhibit relatively poor electrocatalytic activity with an overpotential of about 244 mV, 257 mV and 298 mV at the current densities of 50 mA cm^{-2}, respectively. The results indicated that the addition of Mo could improve the HER catalytic activity of Co/N-CNTs.

The catalytic HER kinetics of all electrocatalysts were also studied using the corresponding Tafel plots, which can be readily determined from the polarization curves by fitting the data into the Tafel equation: $\eta = b\log j + a$, where η is the overpotential, b is the Tafel slope and j is the current density.[36] The Tafel slopes of Co–MoC_x/N-CNT/NF, Co/N-CNT/NF, Co–Cu//N-CNT/NF and Co–Mn_xN_y/N-CNT/NF were found to be 156.08, 152.05, 182.75 and 175.94 mV dec^{-1} (Fig. 2b), respectively. The Tafel slopes of Co–MoC_x/N-CNT/NF and Co/N-CNT/NF are similar and small, which suggest its better HER kinetics and charge transfer rate. The relatively higher Tafel slope indicated that the H_2 release mechanism may be majorly related to the Heyrovsky step. The overpotential and Tafel slope of the catalysts in this work and others are compared and the results are shown in Table S1 (ESI†).

The ECSA of all electrocatalysts was estimated on the basis of C_{dl}. The C_{dl} was estimated using CV scan curves at a potential window of −0.824 to −0.724 V *vs.* Hg/HgO at different scan rates of 20, 40, 60,..., 200 mV s^{-1}. The C_{dl} value was obtained by plotting $\Delta J = (J_a - J_c)$ at −0.774 V *vs.* RHE against the scan rates, and the linear slope is twice the C_{dl} value as shown in Fig. 2c. The ECSA was measured based on the equation (ECSA = C_{dl}/C_S, where C_S is the specific capacitance measured at 0.040 mF cm^{-2}).[37] The details of the calculations and the corresponding results are shown in Table 1. Thus, the ECSA of these catalysts follows the sequence of Co–Mn_xN_y/N-CNT/NF > Co/N-CNT/NF > Co–MoC_x/N-CNT/NF > Co–Cu/N-CNT/NF ≈ NF.

Furthermore, EIS measurements were carried out to understand the HER kinetics and the charge transfer resistance, at the overpotential of 200 mV in 1.0 M KOH electrolyte under HER operating conditions. Their Nyquist plots in the full region are shown in Fig. 2d, then the ohmic resistance (R_s) can be read from a high frequency region, while the charge transfer resistance (R_{ct}) should be quantified using the diameter of the semicircle in the low-frequency zone of the Nyquist plot.[38] The R_{ct} is usually used to assess the kinetics of the electrochemical process on the surface of catalysts.[39] Hence, the R_{ct} obtained from the semicircle in the low-frequency zone is compared. The R_{ct} of Co–MoC_x/N-CNT/NF is calculated to be 5.1 Ω, which was greater than that of Co/N-CNT/NF (3.8 Ω) and Co–Mn_xN_y/N-CNT/NF (3.9 Ω).

In addition, the Faraday efficiency was used to analyze the utilization efficiency of electrons' participation. From Fig. 2e, it can be found that the volume of hydrogen obtained in the experiment is slightly different from the theoretical calculated volume. According to formula (1), the calculated Faraday efficiency for the HER is 99.7%, illustrating that the current was almost attributed to water splitting.

$$\mathrm{FE}(H_2, \%) = \frac{2 \times F \times V_{H_2}}{V_m \times A\int_0^t j\mathrm{d}t} \times 100\% \quad (1)$$

Table 1 Calculation of ECSA for the HER

Electrocatalysts	C_{dl}/mF	ECSA/cm^2
NF	1.83	45.75
Co/N-CNT/NF	33.41	835.30
Co–MoC_x/N-CNT/NF	19.09	477.25
CoMn/N-CNT/NF	37.60	940.00
CoCu/N-CNT/NF	2.19	54.75

where V_{H_2} is the evolved volume of hydrogen, F is the Faraday constant (96485.33289 C mol^{-1}), V_m (24.5 L mol^{-1}) is the molar volume of the gas at room temperature, j is the current density, A is the surface area of the working electrode (1 × 1 cm^2) and t is the time period of electrolysis.

The long-term durability of the Co–MoC$_x$/N-CNT with a constant current density of 10 mA cm^{-2} is tested. After 100 h, the overpotential of the Co–MoC$_x$/N-CNT increased slightly (40 mV), which indicates that the Co–MoC$_x$/N-CNT is relatively stable in a three-electrode system (Fig. S1, ESI†). The turnover frequency (TOF) is commonly used to evaluate the intrinsic activity of the catalyst. The metal contents by mass of the as-synthesized Co–MoC$_x$/N-CNT catalysts determined *via* ICP-OES were found to be 15.1% in Co and 30.0% in Mo. Therefore, it is known that 2 mg of metal contains 0.700 mg of Co and 1.300 mg of Mo, while the total molar amount of Co and Mo is 0.0254 mmol. To avoid difficulties in distinguishing the activity of different sites, it was assumed that all Mo and Co atoms were active sites of the HER in Co–MoC$_x$/N-CNTs. Then, according to formula (2), TOF lower limit values can be calculated. Similarly, the TOF lower limit values of other catalysts can also be calculated (Fig. 2f).

$$\mathrm{TOF} = \frac{j \times A}{2 \times F \times n} \times \mathrm{FE} \quad (2)$$

where j is the current density, A is the surface area of the working electrode (1 × 1 cm^2), F (96485.33289 C mol^{-1}) is the Faraday constant, and the number of 2 means two electrons per H_2 molecule and n is the total molar number of metal ions calculated according to the loading density of the catalyst, and FE is the Faraday efficiency.

The TOF value of the Co–MoC$_x$/N-CNT/NF is 10.208 s^{-1}, which is several times greater than that of the other electrocatalysts (the TOF values of Co/N-CNT/NF, Co–Cu/N-CNT/NF and Co–Mn$_x$N$_y$/N-CNT/NF are 6.665, 3.493 and 5.647 s^{-1}, respectively) at −0.234 V *vs.* RHE (current density is 50 mA cm^{-2} for Co–MoC$_x$/N-CNT/NF). The TOF value of the Co–MoC$_x$/N-CNT/NF is the highest, which suggests its highest intrinsic activity.

Structural characterization of Co–MoC$_x$/N-CNT

FE-SEM images of the catalyst exhibited a relatively regular smooth petal-shape with the thickness of tens of nanometers, which can be observed from Fig. 3a. For the high magnification SEM images as shown in Fig. 3b and c, the interconnected nano-petals with large diameters and ultrathin thickness were grown on the carbon substrate, forming a highly porous architecture.[40] Such an open structure is beneficial for the effective electron transport at the electrode/electrolyte interface. As shown in Fig. 3b, c and Fig. S2 (ESI†), the carbon nanofibers have an average diameter of 17.5 nm, with an aspect ratio of over ten, and they are coated with Co–MoC$_x$ nanoparticles. The Co–MoC$_x$ nanoparticles are generally uniformly distributed and uniform in size, with an average diameter of 14.8 nm (Fig. S2, ESI†). As can be seen from the EDS-mappings (Fig. 3d, e and g, h), the element Mo is mainly distributed on the nanopetals, and the nanoparticles on the nanofibres are mainly formed by Co. Such distributions suggest that the process

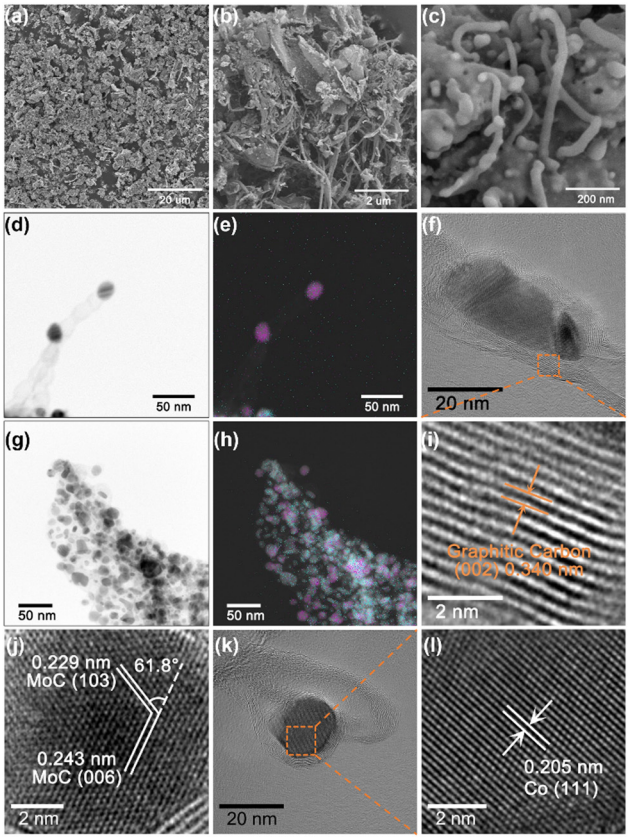

Fig. 3 Structural characterizations of the Co–MoC$_x$/N-CNT catalyst: (a)–(c) FE-SEM images showing the earthworm-like morphology; (d), (e), (g) and (h) STEM-EDS mappings; (f) and (k) TEM images; HRTEM image of (i) the graphitic carbon layers, (j) MoC NP and (l) Co NP.

of g-C$_3$N$_4$ pyrolysis and its transformation to form N-CNTs is closely related to catalysis by Co, whereas Mo is not equipped with this catalytic function. Detailed crystalline structures of graphitic carbon and Co–MoC$_x$ are shown in Fig. 3f and Fig. 3i–l. The (002) lattice plane of graphitic carbon can be clearly seen from Fig. 3i, with a d-spacing of around 3.40 Å. Fig. 3k shows a Co nanoparticle wrapped with several layers of graphitic carbon. The lattice fringes with lattice distances of 2.05 Å correspond to the Co (111) lattice plane shown in Fig. 3l. In Fig. 3j, the lattice fringes with lattice distances of 2.29 Å and 2.43 Å correspond to the MoC (103) and MoC (006) facets, respectively. According to formula (3) and the information of PDF card ICDD No. 89-4305, the dihedral angle of the (006) and (103) planes is calculated to be 61.8°, which is consistent with the result presented *via* HRTEM.

$$\cos\varphi = \frac{h_1h_2 + k_1k_2 + \frac{1}{2}(h_1k_2 + k_1h_2) + \frac{3a^2}{4c^2}l_1l_2}{\sqrt{\left(h_1^2 + k_1^2 + h_1k_1 + \frac{3a^2}{4c^2}l_1^2\right)\left(h_2^2 + k_2^2 + h_2k_2 + \frac{3a^2}{4c^2}l_2^2\right)}} \quad (3)$$

where φ is the degree of dihedral angle between plane (h_1 k_1 l_1) and plane (h_2 k_2 l_2) and a, a and c are the three edge lengths of the unit cell.

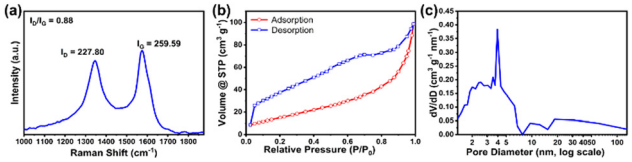

Fig. 4 (a) Raman spectrum; (b) isothermal curves and (c) pore size distributions of the Co–MoC$_x$/N-CNT.

The Raman spectrum of the catalyst was also used to identify structural defects and transformations, as presented in Fig. 4a. The D-band at 1346 cm^{-1} was aroused due to structural deformations by sp^3-hybridizied carbon vibrations, while the G-band at 1576 cm^{-1} originated from the E_{2g} scattering vibrational mode of first-ordered Raman scattering in the hexagonal lattice by the C–C bond in the graphitic structure. The ratio of I_D/I_G was determined to be 0.88, which suggests a high degree of defect in the catalyst likely caused by Co and Mo dopants in the structures. The surface area and porosity of the catalyst support were measured using nitrogen adsorption–desorption isotherms, as shown in Fig. 4b. The absorption–desorption isotherm displayed a clear hysteresis look of a type IV isotherm according to the International Union of Pure and Applied Chemistry (IUPAC) nomenclature with a specific surface area S_{BET} of 162 m^2 g^{-1}, while the total pore volume of the material was determined to be 0.16 cm^3 g^{-1}. Based on the BJH methods, the average pore size diameter of the micropores was about 3.94 nm, as displayed in Fig. 4c. It is believed that the high porosity provides a greater surface area of active Co and Mo sites leading to higher reactivities.

The surface elemental composition and metal valence of Co–MoC$_x$/N-CNTs were determined *via* XPS as shown in Fig. 5, while the peaks of the catalyst were mainly attributed to the Co 2p, Mo 3d, C 1s, N 1s and O 1s regions (Fig. 5a). The XPS spectrum of Co 2p$_{3/2}$ was deconvoluted into two peaks: a metallic Co peak at 778.7 eV and a Co–O$_x$ peak at 780.7 eV. The spectrum of Co 2p$_{1/2}$ was deconvoluted into two peaks: a metallic Co peak at 794.0 eV and a Co–O$_x$ peak at 796.0 eV (Fig. 5b). The Mo 3d spectrum in Fig. 5c reveals that there are three states (+δ, +4 and +6) for Mo in Co–MoC$_x$/N-CNTs. The valence of Mo in MoC is mainly +4, and the peak at 228.7 eV is associated with the Mo 3d$_{5/2}$ in MoC and attributed to the carbide phase. The multiple valence peaks of Mo$^{\delta+}$ ($0 \leq \delta \leq 4$) may be attributed to the presence of Mo_2C (resulting from the partial carbonization of MoC). In addition, the Mo–O species (Mo^{6+}) may be arisen from the surface oxidation when the sample was exposed to the air.[41,42] The spectrum of C 1s was deconvoluted into two peaks, where the peaks at 284.8 and 285.2 eV were attributed to the C–C (sp^2) and C–C (sp^3) bonds, respectively (Fig. 5d). The presence of a N-dopant was confirmed by the peak at 286.1 eV[43] and the broad peak at 290.4 eV indicated some surface oxidation of carbon atoms. The peaks located at the binding energy of 283.5 eV can be attributed to the Mo–C species.[42] The high resolution of N 1s can be deconvoluted into three peaks, which were the C–N–C (pyridinic N), C–N–H (pyrrolic N) and C–N (graphitic N) peaks at 398.5, 400.0 and 399.5 eV, respectively (Fig. 5e). Lastly, the O 1s spectrum displayed a broad peak which

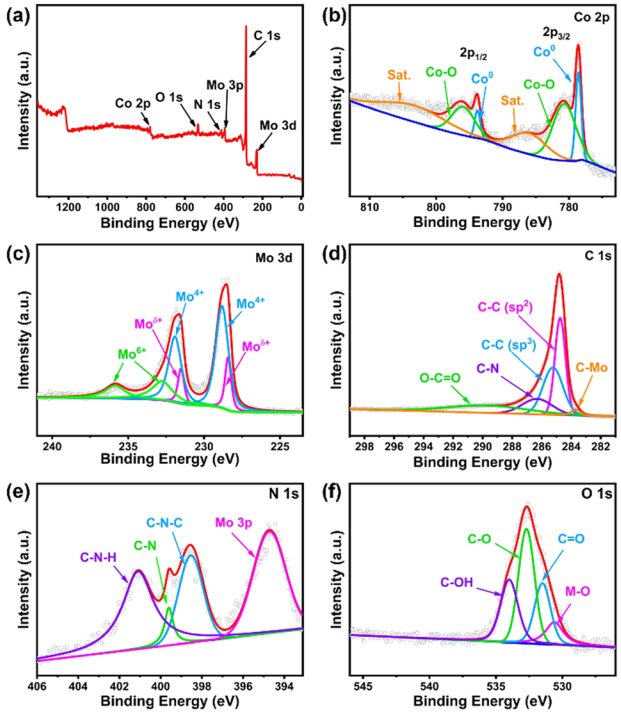

Fig. 5 High resolution XPS spectra of the as-synthesized Co–MoC$_x$/N-CNT catalyst: (a) survey spectrum; (b) Co 2p; (c) Mo 3d; (d) C 1s; (e) N 1s; (f) O 1s.

was assigned to Co–O and Mo–O (530.6 eV), C═O (531.5 eV), C–O (532.7 eV) and C–OH (534.0 eV) (Fig. 5f).[44]

Conclusions

Under the same pyrolytic conditions and ratio of metal salt precursors (Co paired up with Mo, Mn and Cu, respectively) to *melem*-C_3N_4 (DCD-350), various forms of bimetallic NPs supported on CNTs were formed. Molybdenum carbides are preferentially formed while manganese nitrides are almost exclusively formed. Pairing up Co NPs with MoC$_x$ boosted the HER activity by more than 2-fold (η_{10} = 130 mV, Tafel slope = 156.08 mV dec^{-1}), compared with the pure Co NPs supported on N-doped carbon (η_{10} = 337 mV) under alkaline conditions. The activity is comparable to Pt SACs supported on a mesoporous carbon matrix. The charge transfer resistance (R_{ct}) of the Co–MoC$_x$/N-CNT/NF is calculated to be 5.1 Ω, demonstrating the fast kinetics of the electrochemical process on the surface of catalysts. The TOF value of the Co–MoC$_x$/N-CNT/NF was found to be 10.208 s^{-1}, which suggested its highest intrinsic activity. The good activity may be due to the modification of the D-band of Co by Mo doping and the relatively high ECSA of 477.25 cm^2, which is comparable to Ru SAC materials.

Author contributions

Weilin Shen: data curation, formal analysis, investigation, writing – original draft. Dawson Wai-Shun Suen: structural characterization, writing – original draft, data curation,

validation, visualization. Eric Tung-Po Sze: structural characterization. Xiao Chen: validation, writing – original draft. Changhai Liang: conceptualization, investigation, visualization, funding acquisition, supervision. Chi-Wing Tsang: conceptualization, funding acquisition, methodology, project administration, resources, supervision, validation, structural characterization, visualization, writing – original draft, writing – review and editing.

Conflicts of interest

There are no conflicts to declare.

Acknowledgements

This work was fully funded by the Hong Kong University Grants Committee – the Faculty Development Scheme (FDS), grant number UGC/FDS25/E08/20, UGC/FDS25/E04/22 and partially funded by the Institutional Development Scheme (IDS), grant number UGC/IDS(R)25/20 and the National Natural Science Foundation of China, grant number 22161132005, 22172016 and 22272014.

Notes and references

1 Z.-Y. Zhang, H. Tian, L. Bian, S.-Z. Liu, Y. Liu and Z.-L. Wang, *J. Energy Chem.*, 2023, **83**, 90–97.
2 M. Luo, J. Yang, X. Li, M. Eguchi, Y. Yamauchi and Z. L. Wang, *Chem. Sci.*, 2023, **14**, 3400–3414.
3 J. Mahmood, F. Li, S.-M. Jung, M. S. Okyay, I. Ahmad, S.-J. Kim, N. Park, H. Y. Jeong and J.-B. Baek, *Nat. Nanotech.*, 2017, **12**, 441–446.
4 M. Zhang, D. Hu, Z. Xu, B. Liu, M. Boubeche, Z. Chen, Y. Wang, H. Luo and K. Yan, *J. Mater. Sci. Technol.*, 2021, **72**, 172–179.
5 Y. He, T. L. Wang, M. Zhang, T. W. Wang, L. F. Wu, L. Zeng, X. Wang, M. Boubeche, S. Wang, K. Yan, S. H. Lin and H. Luo, *Small*, 2021, **17**, e2006153.
6 Y. He, M. Boubeche, Y. Zhou, D. Yan, L. Zeng, X. Wang, K. Yan and H. Luo, *J. Phys: Mater*, 2020, **4**, 14001–14008.
7 T. Chao, X. Luo, W. Chen, B. Jiang, J. Ge, Y. Lin, G. Wu, X. Wang, Y. Hu, Z. Zhuang, Y. Wu, X. Hong and Y. Li, *Angew. Chem., Int. Ed.*, 2017, **56**, 16047–16051.
8 F. Neuberger, J. Baranyai, T. Schmidt, T. Cottre, B. Kaiser, W. Jaegermann and R. Schäfer, *Z. fur Phys. Chem.*, 2020, **234**, 847–865.
9 B. Qiao, A. Wang, X. Yang, L. F. Allard, Z. Jiang, Y. Cui, J. Liu, J. Li and T. Zhang, *Nat. Chem.*, 2011, **3**, 634–641.
10 N. Cheng, S. Stambula, D. Wang, M. N. Banis, J. Liu, A. Riese, B. Xiao, R. Li, T. K. Sham, L. M. Liu, G. A. Botton and X. Sun, *Nat. Commun.*, 2016, **7**, 13638.
11 H. Zhang, P. An, W. Zhou, B. Y. Guan, P. Zhang, J. Dong and X. W. D. Lou, *Sci. Adv.*, 2018, **4**, eaao6657.
12 H. Fei, Y. Yang, Z. Peng, G. Ruan, Q. Zhong, L. Li, E. L. Samuel and J. M. Tour, *ACS Appl. Mater. Interfaces*, 2015, **7**, 8083–8087.
13 Y.-Y. Ma, C.-X. Wu, X.-J. Feng, H.-Q. Tan, L.-K. Yan, Y. Liu, Z.-H. Kang, E.-B. Wang and Y.-G. Li, *Energy Environ. Sci.*, 2017, **10**, 788–798.
14 M. Feng, J. Huang, Y. Peng, C. Huang, X. Yue and S. Huang, *Chem. Eng. J.*, 2022, **428**, 131206–131214.
15 B. Cao, G. M. Veith, J. C. Neuefeind, R. R. Adzic and P. G. Khalifah, *J. Am. Chem. Soc.*, 2013, **135**, 19186–19192.
16 Y. Yuan, S. Adimi, T. Thomas, J. Wang, H. Guo, J. Chen, J. P. Attfield, F. J. DiSalvo and M. Yang, *Innovation*, 2021, **2**, 100096.
17 S. Shit, W. Jang, S. Bolar, N. C. Murmu, H. Koo and T. Kuila, *ACS Appl. Mater. Interfaces*, 2019, **11**, 21634–21644.
18 Z. Chen, Y. Song, J. Cai, X. Zheng, D. Han, Y. Wu, Y. Zang, S. Niu, Y. Liu, J. Zhu, X. Liu and G. Wang, *Angew. Chem., Int. Ed.*, 2018, **57**, 5076–5080.
19 Z. Zhang, J. Cai, H. Zhu, Z. Zhuang, F. Xu, J. Hao, S. Lu, H. Li, F. Duan and M. Du, *Chem. Eng. J.*, 2020, **392**, 123655–123663.
20 A. Bulut, M. Yurderi, İ. E. Ertas, M. Celebi, M. Kaya and M. Zahmakiran, *Appl. Catal. B: Environ.*, 2016, **180**, 121–129.
21 X. Zhang, W. Shen, Z. Li, D. Wang, J. Qi and C. Liang, *Carbon*, 2020, **167**, 548–558.
22 Y. Cheng, S. Zhao, B. Johannessen, J. P. Veder, M. Saunders, M. R. Rowles, M. Cheng, C. Liu, M. F. Chisholm, R. De Marco, H. M. Cheng, S. Z. Yang and S. P. Jiang, *Adv. Mater.*, 2018, **30**, e1706287.
23 S. Zhao, Y. Cheng, J.-P. Veder, B. Johannessen, M. Saunders, L. Zhang, C. Liu, M. F. Chisholm, R. De Marco, J. Liu, S.-Z. Yang and S. P. Jiang, *ACS Appl. Energy Mater.*, 2018, **1**(10), 5268–5297.
24 P.-C. Poon, Y. Wang, W. Li, D. W.-S. Suen, W. W. Y. Lam, D. Z. J. Yap, B. L. Mehdi, J. Qi, X.-Y. Lu, E. Y. C. Wong, C. Yang and C.-W. Tsang, *J. Mater. Chem. A*, 2022, **10**, 5580–5592.
25 C. Giordano, C. Erpen, W. Yao and M. Antonietti, *Nano Lett.*, 2008, **8**, 4659–4663.
26 Y. Qiu and L. Gao, *J. Am. Ceram. Soc.*, 2004, **87**, 352–357.
27 R. Subbaraman, D. Tripkovic, D. Strmcnik, K. C. Chang, M. Uchimura, A. P. Paulikas, V. Stamenkovic and N. M. Markovic, *Science*, 2011, **334**, 1256–1260.
28 W. Liu, T. Xia, Y. Ye, H. Wang, Z. Fang, Z. Du and X. Hou, *Int. J. Hydrog. Energy*, 2021, **46**, 27037–27043.
29 Q. Liu, J. Tian, W. Cui, P. Jiang, N. Cheng, A. M. Asiri and X. Sun, *Angew. Chem., Int. Ed.*, 2014, **53**, 6710–6714.
30 J. Duan, S. Chen, B. A. Chambers, G. G. Andersson and S. Z. Qiao, *Adv. Mater.*, 2015, **27**, 4234–4241.
31 Z. Luo, R. Miao, T. D. Huan, I. M. Mosa, A. S. Poyraz, W. Zhong, J. E. Cloud, D. A. Kriz, S. Thanneeru, J. He, Y. Zhang, R. Ramprasad and S. L. Suib, *Adv. Energy Mater.*, 2016, **6**, 1600528.
32 F.-X. Ma, H. B. Wu, B. Y. Xia, C.-Y. Xu and X. W. Lou, *Angew. Chem., Int. Ed.*, 2015, **54**, 15395–15399.
33 Z. Ma, L. Niu, W. Jiang, C. Dong, G. Liu, D. Qu, L. An and Z. Sun, *J. Phys. Mater.*, 2021, **4**, 42002–42018.

34 D. Liu, X. Li, S. Chen, H. Yan, C. Wang, C. Wu, Y. A. Haleem, S. Duan, J. Lu, B. Ge, P. M. Ajayan, Y. Luo, J. Jiang and L. Song, *Nat. Energy*, 2019, **4**, 512–518.
35 L. Cao, Q. Luo, W. Liu, Y. Lin, X. Liu, Y. Cao, W. Zhang, Y. Wu, J. Yang, T. Yao and S. Wei, *Nat. Catal.*, 2018, **2**, 134–141.
36 Z. X. Cai, H. Goou, Y. Ito, T. Tokunaga, M. Miyauchi, H. Abe and T. Fujita, *Chem. Sci.*, 2021, **12**, 11306–11315.
37 C. C. McCrory, S. Jung, J. C. Peters and T. F. Jaramillo, *J. Am. Chem. Soc.*, 2013, **135**, 16977–16987.
38 P. Wang, J. Qi, C. Li, X. Chen, J. Luo, W. Li, X. Shi, L. Olivet, T. Wang and C. Liang, *Int. J. Hydrogen Energy*, 2019, **44**, 14955–14967.
39 Y. Wang, Y. Zhu, S. Afshar, M. W. Woo, J. Tang, T. Williams, B. Kong, D. Zhao, H. Wang and C. Selomulya, *Nanoscale*, 2019, **11**, 3500–3505.
40 T. Peng, H. Yi, P. Sun, Y. Jing, R. Wang, H. Wang and X. Wang, *J. Mater. Chem. A*, 2016, **4**, 8888–8897.
41 T. Chen, X. Yan, Z. Ma, Y. Zhang, X. Zheng and Y. Jiang, *Ionics*, 2020, **26**, 4869–4875.
42 H.-Q. Chang, G.-H. Zhang and K.-C. Chou, *Electrochim. Acta*, 2021, **394**, 139119–139127.
43 X. Ge, Z. Li and L. Yin, *Nano Energy*, 2017, **32**, 117–124.
44 Q. Jia, Y. Gao, Y. Li, X. Fan, F. Zhang, G. Zhang, W. Peng and S. Wang, *Carbon*, 2019, **155**, 287–297.